

# Nitrogen and Sulfur Co-Doped Hierarchically Porous Carbon Nanotubes for Fast Potassium Ion Storage

Xin Jin, Xianfen Wang, Yalan Liu, Minjun Kim, Min Cao, Huanhuan Xie,\* Shantang Liu, Xianbao Wang, Wei Huang, Ashok Kumar Nanjundan, Brian Yulianto, Xingyun Li,\* and Yusuke Yamauchi\*

Exploration of advanced carbon anode material is the key to circumventing the sluggish kinetics and poor rate capability for potassium ion storage. Herein, a synergistic synthetic strategy of engineering both surface and structure is adopted to design N, S co-doped carbon nanotubes (NS-CNTs). The as-designed NS-CNTs exhibit unique features of defective carbon surface, hollow tubular channel, and enlarged interlayer space. These features significantly contribute to a large potassium storage capacity of 307 mA h g<sup>-1</sup> at 1 A g<sup>-1</sup> and a remarkable rate performance with a capacity of 151 mA h g<sup>-1</sup> even at 5 A g<sup>-1</sup>. Furthermore, an excellent cyclability with 98% capacity retention after 500 cycles at 2 A g<sup>-1</sup> is also achieved. Systematic analysis by in situ Raman spectroscopy and ex situ TEM demonstrates the structural stability and reversibility in the charge–discharge process. Although the kinetics studies reveal the capacitive-dominated process for potassium storage, density functional theory calculations provide evidence that N, S co-doping contributes to expanding the interlayer space to promote the K-ion insertion, improving the electronic conductivity, and providing ample defective sites to favor the K-ion adsorption.

## 1. Introduction

The development of advanced energy storage technologies holds great importance to promote the implementation of renewable energies.<sup>[1–3]</sup> Lithium-ion batteries (LIBs) have been successfully commercialized as the mainstream energy storage device in the market in recent years.<sup>[4–6]</sup> However, the large-scale application of LIBs is severely restricted by the drawbacks such as low cell voltage, high price, and resource scarcity of lithium.<sup>[7,8]</sup> As alternative energy storage, potassium-ion batteries (KIBs) have attracted extensive attention.<sup>[9,10]</sup> However, the KIBs often suffer from the huge volume changes and poor kinetics induced by the larger ionic radius of K<sup>+</sup> (1.38 Å).<sup>[9]</sup> To address the above issues, the development of advanced anode materials to ensure satisfying

X. Jin, X. Wang, M. Cao, X. Li  
Institute of Materials for Energy and Environment  
College of Materials Science and Engineering  
Qingdao University  
Qingdao 266071, China  
E-mail: xingyun\_2008@sina.cn

Y. Liu, S. Liu  
Key Laboratory for Green Chemical Process of Ministry of Education  
School of Chemistry and Environmental Engineering  
Wuhan Institute of Technology  
Wuhan 43000, China

M. Kim, A. K. Nanjundan, Y. Yamauchi  
Australian Institute for Bioengineering and Nanotechnology (AIBN)  
and School of Chemical Engineering  
The University of Queensland  
Brisbane, Queensland 4072, Australia  
E-mail: yamauchi.yusuke@nims.go.jp

H. Xie  
School of Chemistry and Material Science  
Shanxi Normal University  
Xi'an 710000, China  
E-mail: xiehh17@pku.edu.cn


X. Wang  
Ministry-of-Education Key Laboratory for the Green Preparation  
and Application of Functional Materials  
Hubei University  
Wuhan 430062, China

W. Huang  
Key Laboratory of Coal Science and Technology  
Education Ministry and Shanxi Province  
Taiyuan University of Technology  
Taiyuan, Shanxi 030024, China

B. Yulianto  
Advanced Functional Materials (AFM) Laboratory  
Engineering Physics Department  
Institut Teknologi Bandung  
Bandung 40132, Indonesia

B. Yulianto  
Research Center for Nanosciences and Nanotechnology (RCNN)  
Institute of Technology Bandung  
Bandung 40132, Indonesia

Y. Yamauchi  
International Center for Materials Nanoarchitectonics (WPI-MANA)  
National Institute for Materials Science (NIMS)  
1-1 Namiki, Tsukuba, Ibaraki 305-0044, Japan

 The ORCID identification number(s) for the author(s) of this article can be found under <https://doi.org/10.1002/smll.202203545>.

© 2022 The Authors. Small published by Wiley-VCH GmbH. This is an open access article under the terms of the Creative Commons Attribution License, which permits use, distribution and reproduction in any medium, provided the original work is properly cited.

DOI: 10.1002/smll.202203545

structure stability as well as stable and high capacity is under active research.<sup>[10,11]</sup>

Up to now, different kinds of anode materials have been explored, for example, carbon, metal oxide, sulfide, selenide, and phosphide.<sup>[4,12–15]</sup> Among them, carbonaceous materials have been a preferred choice of material due to their excellent electrical conductivity, eco-friendliness, wide availability, and cost-competitiveness.<sup>[16–18]</sup> Tremendous efforts have been, therefore, devoted to the surface and structure modifications to achieve high-performance carbon anode materials. Among various surface modifications, surface heteroatom doping has been demonstrated as an efficient method to improve electrochemical performance. For instance, nitrogen (N) doping contributes to improving electronic conductivity, increasing surface hydrophilicity, and providing abundant defective sites for K-ion storage.<sup>[19,20]</sup> Alternatively, heteroatom doping with sulfur (S) atom, which is larger in size and less electronegative than the N, effectively enlarges the interlayer space and creates structure defects by forming C–S bonds, therefore, achieving a significant increase in the capacity.<sup>[19,20]</sup> The porous structure is important to improve the kinetic process, promote contact with the electrolyte, and offer abundant active sites for pseudocapacitance in K-ion storage. Specifically, engineering a hollow porous architecture with unique cavities is particularly intriguing not only for surface exposure but also for the alleviation of structure destruction during cycling.<sup>[16,21–23]</sup> For example, 1D carbon nanotubes derived from polyamine achieved remarkable cycling stability by retaining the reversible capacity of 168 mA h g<sup>-1</sup> at 2 A g<sup>-1</sup> over 3000 cycles.<sup>[21]</sup> MOF-derived hollow carbon nanobubbles were also reported to provide a shortened diffusion pathway and offer a more accessible active surface to ensure a fast K ion interaction.<sup>[24]</sup>

Herein, we integrate the beneficial surface and structural properties into one system of the carbon nanotube co-doped

with N and S atoms. Typically, a metal sulfide nanowire is adopted as both the sacrificing template and the sulfur source to synthesize N, S co-doped carbon nanotube. The unique hollow and hierarchical porosity, highly exposed defect sites, and expanded interlayer space act interactively to achieve an impressive specific capacity and excellent cycling stability. By systematic in situ/ex situ characterizations, kinetic analysis, and DFT calculations, the synergistic effect of surface and structure for boosting electrical performance is elucidated. This study, therefore, demonstrates a facile methodology to advance carbons as anode materials in future KIBs.

## 2. Results and Discussion

To synthesize N, S co-doped carbon nanotube (NS-CNT), CdS nanowire was used as the structure-directing template. **Figure 1a** shows that CdS is in a wire-like morphology with a diameter of  $\approx 80$  nm. Dopamine was then subjected to in situ polymerization on the surface of CdS to form a 1D core-shell structure, in which CdS was evenly encapsulated by polymerized dopamine (PDA) (**Figure 1b**). Urea-assisted pyrolysis was subsequently carried out to trigger the carbonization and N incorporation to form N-doped carbon (CN) layers. In the process of carbonization, CdS tends to decompose at temperatures above 800 °C, as evidenced by the TGA results in **Figure S1**, Supporting Information. The decomposition of CdS, therefore, leads to the formation of tubular structure without the post-treatment to remove the template. In addition, S species from the decomposing CdS are simultaneously introduced into the carbon layers, resulting in the S doping in the CN layer during the calcination process. TEM and SEM images of NS-CNT-1000 in **Figure 1c,d** demonstrate the nanotube morphology with an outer diameter of  $\approx 100$  nm and inner diameter of  $\approx 80$  nm, which matches well

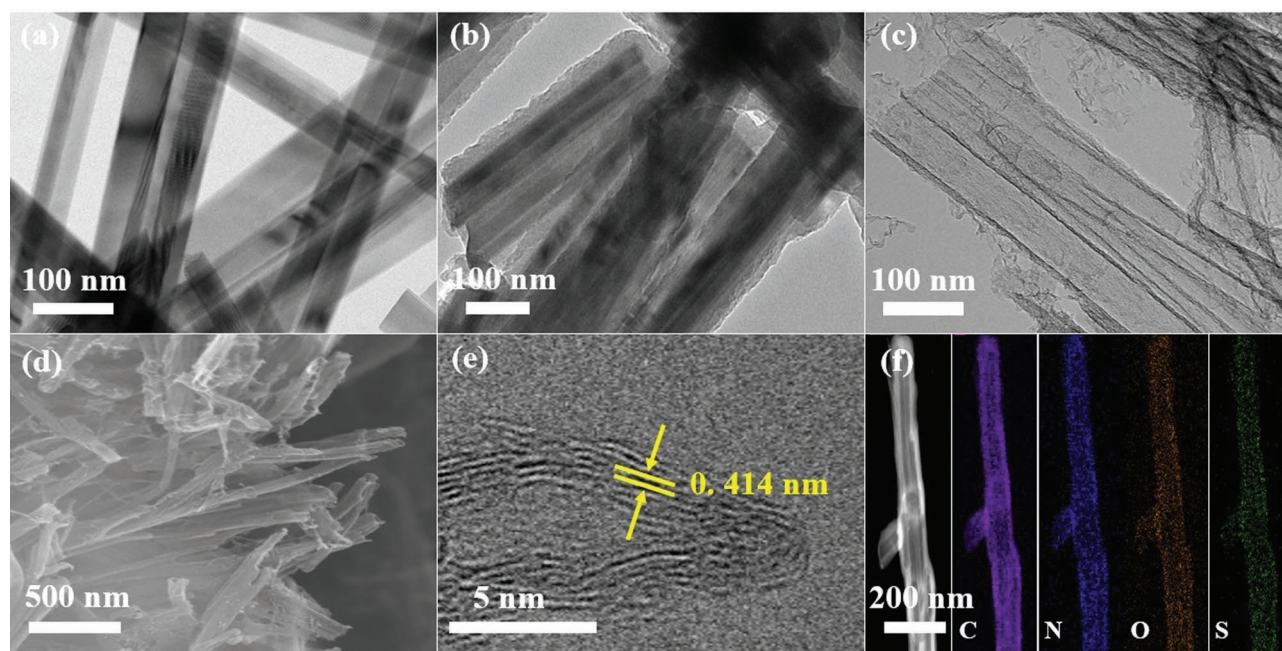


**Figure 1.** Morphologies of intermediate and final products. a) TEM of CdS nanowires, b) TEM of CdS@PDA, c) TEM, d) SEM, e) HR-TEM, and f) STEM and the EDX elemental mapping for NS-CNT-1000.

with the diameter of CdS nanowires (Figure 1a). The tubular structure is also evident for NS-CNT-900 and NS-CNT-1100 as shown in Figure S2, Supporting Information. However, NS-CNT-900 presents a rougher structure with residual CdS on the surface, suggesting that CdS is partially decomposed at the low temperature of 900 °C. HR-TEM image in Figure 1e indicates that NS-CNT-1000 is composed of partially graphitized carbon flakes with lattice spacing of 0.414 nm, which is obviously wider than that of graphite (0.348 nm). The expansion of interlayer distance is potentially due to the presence of heteroatoms, especially the large S atom, doped in the carbon network. STEM and EDX elemental mapping images in Figure 1f demonstrate a homogeneous distribution of C, O, N, and S throughout the framework of NS-CNT-1000, suggesting the uniform co-doping of N and S. A negligible signal of Cd can be detected, suggesting that Cd is successfully removed in NS-CNT-1000 (Figure 1f). The N, S co-doped hollow tubular structure is also observed for NS-CNT-900 (Figure S3, Supporting Information). The above results, therefore, successfully highlight the feasibility of using CdS not only as the structural template but also as the source of S to construct the N, S co-doped carbon nanotubes.

XRD patterns in Figure 2a show one single peak at around 24° for NS-CNT-1000 and NS-CNT-1100, corresponding to the characteristic diffraction of the (002) plane of carbon materials.<sup>[25,26]</sup> For NS-CNT-900, there also present extra XRD peaks at 26.2°, 31.8°, 37.0°, and 45.7°, which are assignable to the CdS crystals (PDF No.43-0985). This suggests that CdS is completely removed at temperature above 1000 °C, but it partially remains at 900 °C. Figure 2b demonstrates two typical Raman peaks at

1580 cm<sup>-1</sup> and 1350 cm<sup>-1</sup>, corresponding to G and D bands of carbon materials, respectively.<sup>[27,28]</sup> The D band represents the disordered carbon structure, while the G band reflects the presence of sp<sup>2</sup> hybridization of carbon atoms (aromatic rings and conjugated chains). A higher ratio of I<sub>D</sub>/I<sub>G</sub>, therefore, indicates poor graphitization of the carbon material. From Figure 2b, I<sub>D</sub>/I<sub>G</sub> value tends to decrease with the rise of calcination temperature from 900 °C to 1100 °C, indicating that a higher level of graphitization can be achieved at the higher temperature.

As the pore volume and the surface area are significant factors influencing the K-ion storage performance, N<sub>2</sub> sorption isotherms were measured.<sup>[29]</sup> The N<sub>2</sub> sorption isotherms of NS-CNT-*T* are shown in Figure 2c. The obvious N<sub>2</sub> uptake at a relative pressure of  $P/P_0 < 0.1$  suggests the existence of micropores in the structure.<sup>[30,31]</sup> The resulting NLDFT pore size distributions (Figure 2d) further corroborate the hierarchical pore structures of NS-CNT-*T*, displaying that the pores are mainly distributed at 0.7, 1.4, and 2.9 nm. According to Table 1, NS-CNT-900 has the specific surface area (SSA) and pore volume of NS-CNT-900 is 569.9 m<sup>2</sup> g<sup>-1</sup> and 2.2 cm<sup>3</sup> g<sup>-1</sup>, respectively. The calcination at 1000 °C boosts the SSA to 754.1 m<sup>2</sup> g<sup>-1</sup>, derived from the conspicuous increase in the micropore volume (Figure 2d). The SSA and pore volume, however, decrease remarkably upon the further increase of calcination temperature to 1100 °C. This may be due to the pore collapse and blockage at such a high calcination temperature.

Figure 3a shows the survey XPS spectrum of NS-CNT-1000, demonstrating the presence of C, O, N, and S elements. N and S doping levels of NS-CNT-1000 are calculated to be 4.0 at% and 1.3 at%, respectively. This is slightly lower than that of NS-CNT-900,

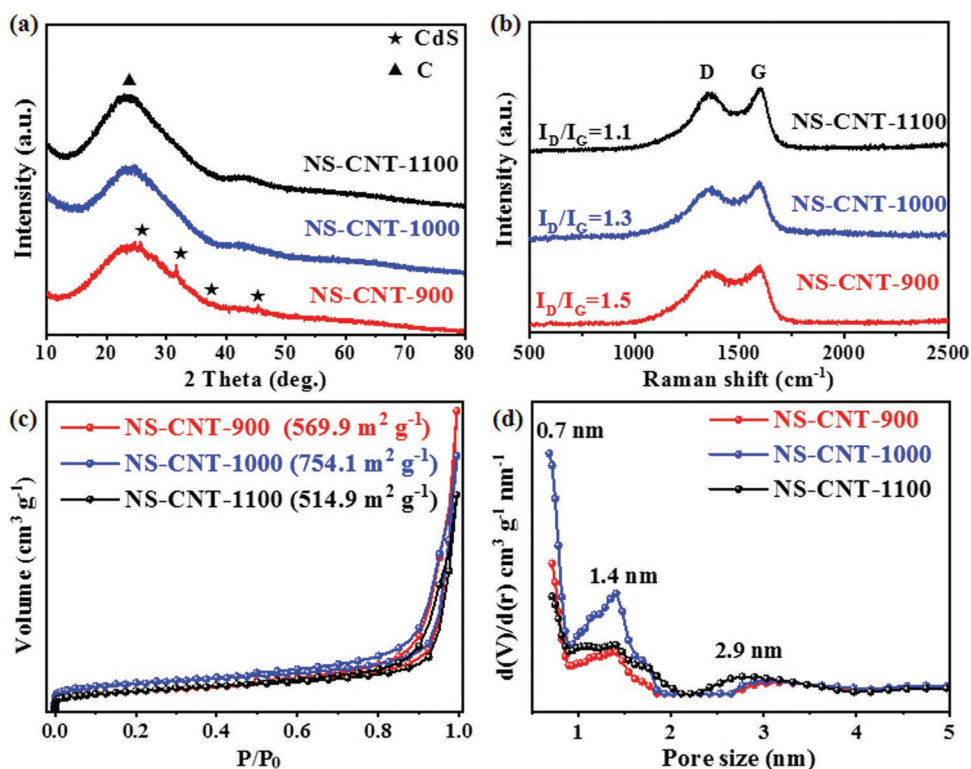


Figure 2. a) XRD pattern, b) Raman pattern, c) N<sub>2</sub> sorption isotherms, and d) NLDFT pore size distribution of NS-CNT-*T*.

**Table 1.** Pore structure and surface information of NS-CNT-*T*.

Sample	<sup>a)</sup> SSA [m <sup>2</sup> g <sup>-1</sup> ]	<sup>b)</sup> V <sub>total</sub> [cm <sup>3</sup> g <sup>-1</sup> ]	<sup>c)</sup> V <sub>micro</sub> [cm <sup>3</sup> g <sup>-1</sup> ]	Atomic percentage [at%]			
				C	N	O	S
NS-CNT-900	569.9	2.2	0.06	89.3	4.8	4.3	1.6
NS-CNT-1000	754.1	3.2	0.14	90.3	4.0	4.4	1.3
NS-CNT-1100	514.9	1.7	0.07	95.1	2.4	2.2	0.3

<sup>a)</sup>SSA: specific surface area; <sup>b)</sup>V<sub>total</sub>: total pore volume; <sup>c)</sup>V<sub>micro</sub>: micropore volume.

but obviously higher than that of NS-CNT-1100 (Table 1; Figures S4 and S5, Supporting Information). This suggests that the doping level of N and S is temperature sensitive and a higher calcination temperature may hamper the successful heteroatom doping in the carbon network at a higher level. As shown in Figure 3b, high-resolution XPS (HR-XPS) spectrum for C 1s of NS-CNT-1000 can be deconvoluted by four characteristic peaks at 289.9, 287.3, 285.8, and 284.8 eV, which represent O=C–O, C–S, C–N, and C–C bond, respectively.<sup>[32–34]</sup> The deconvoluted XPS spectra for N 1s are presented in Figure 3c, in which the peaks represent the oxidized-N (N-O), quaternary-N (N-Q), pyrrolic-N (N-5), and pyridinic-N (N-6).<sup>[32,35]</sup> The quaternary N and pyrrolic-N are known to play an important role for the enhancement of electrical conductivity, and the K ion adsorption, respectively.<sup>[36,37]</sup> Among the NS-CNT-*T* samples, NS-CNT-1000 consists of the highest ratio of pyrrolic-N species; hence, potentially serving as the optimized anode material for KIB (Figures S4 and S5 and Table S1, Supporting Information).

The XPS spectra for S 2*p* of NS-CNT-1000 in Figure 3d is composed of three peaks, of which 164.9 and 163.9 eV correspond to C–S–C bonds, and 168.0 eV corresponds to oxidized-S (S-O).<sup>[38–40]</sup> The chemical bonding of large-sized S atom in the lattice potentially explains the expanded interlayer distance observed from the HR-TEM image of NS-CNT-1000 (Figure 1e). Based on the above characterizations, the synergistic effect of N and S co-doping in the NS-CNT results in the large interlayer distance, hierarchical pore structure, and defective surface; hence likely to improve the electrochemical performance of K ion storage.

Electrochemical profiles in Figure 4a demonstrate the galvanostatic charge–discharge (GCD) curve of NS-CNT-1000 at 0.02 A g<sup>-1</sup> in 0.01–3.0 V (vs K/K<sup>+</sup>). It displays an ultra-high initial discharge and charge capacities of 2868 and 397 mA h g<sup>-1</sup>, respectively. The irreversible capacity loss is potentially induced by the generation of the solid electrolyte interphase (SEI) layer, leading to a low initial Coulombic efficiency of 18.7%. The CV profiles in

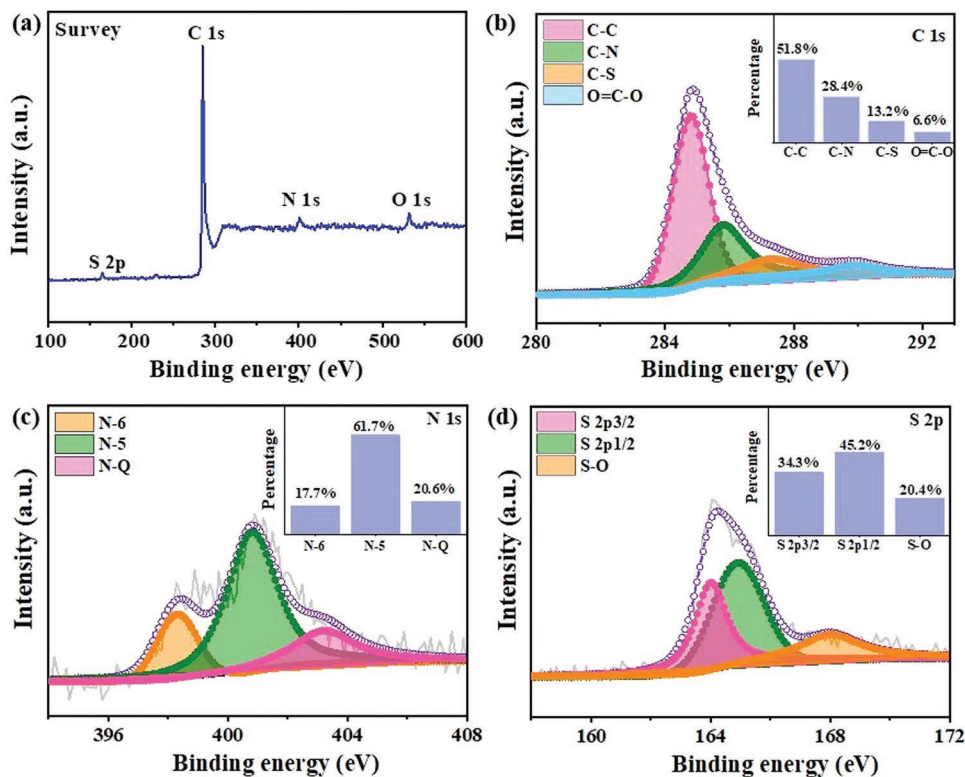


**Figure 3.** a) Survey XPS spectrum of NS-CNT-1000. HRXPS spectrum for b) C 1s, c) N 1s, and d) S 2*p* of NS-CNT-1000 (the inset shows the proportions of different types of C, N, and S).

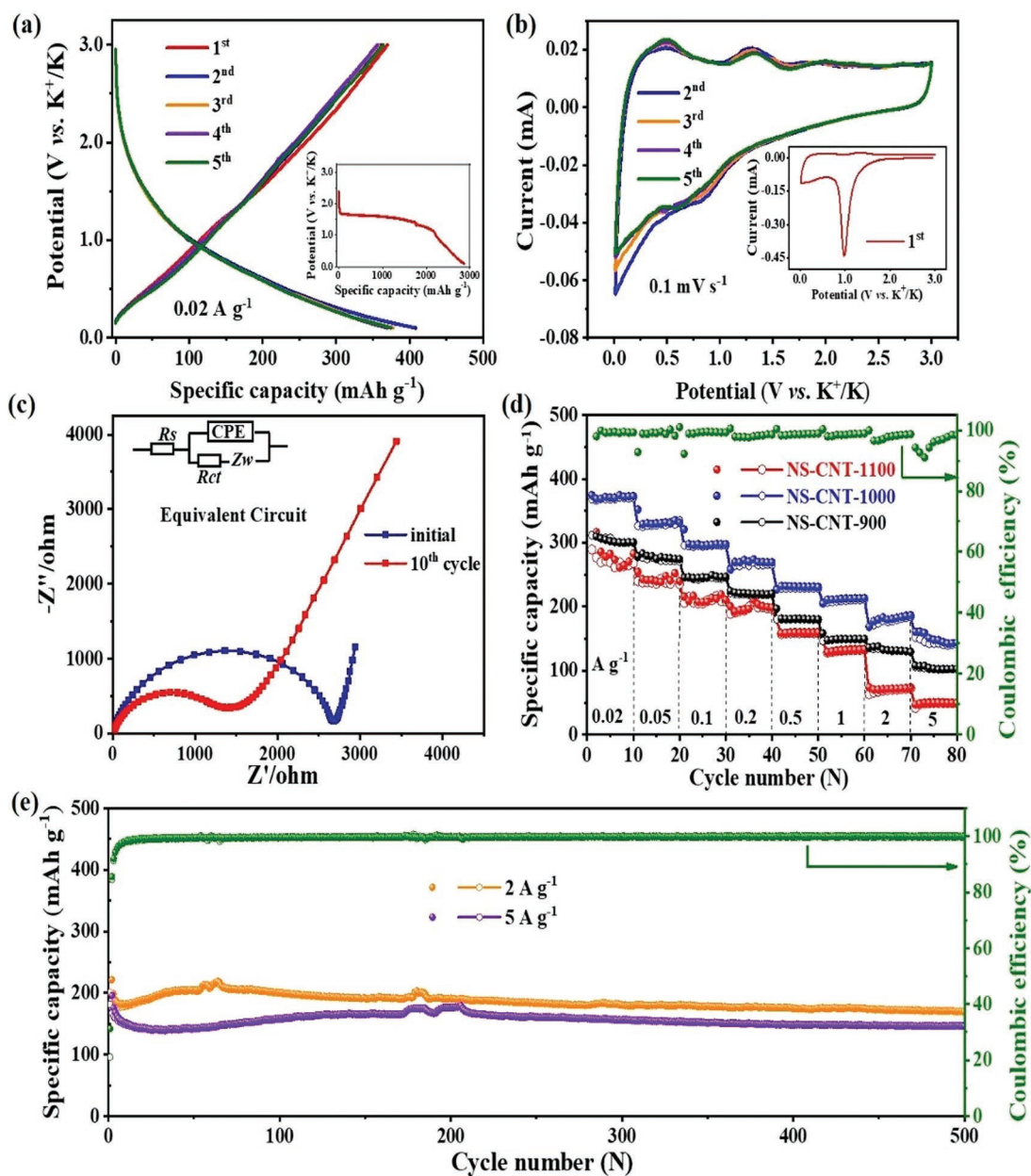


**Figure 4.** a) Galvanostatic charge/discharge profiles of NS-CNT-1000 at  $0.02 \text{ A g}^{-1}$ , b) CV curves of NS-CNT-1000 at a scan rate of  $0.1 \text{ mV s}^{-1}$ , c) Nyquist plots of NS-CNT-1000 (the inset is the equivalent circuit), d) rate capabilities and Coulombic efficiency of NS-CNT-1000, e) the cyclic stability of NS-CNT-1000 at  $2.0$  and  $5.0 \text{ A g}^{-1}$ .

Figure 4b reveal distinct cathodic peaks for the NS-CNT-1000 in the first cycle recorded at  $0.1 \text{ mV s}^{-1}$ . The obvious cathodic peak at  $1.0 \text{ V}$  could be attributed to the SEI layer formation and K-ions trapping in the carbon matrix,<sup>[12,41]</sup> while the cathodic peak around  $0.01 \text{ V}$  could be related to the K-ion insertion/extraction processes in the carbon interlayers. The subsequent CV curves with high reversibility suggest the superior structural robustness of NS-CNT-1000 as anode material during K-ion insertion/extraction. The decreased diameter of semicircles in Nyquist plots of initial and 10th cycles indicates that the charge transfer resistance is reduced upon the repeated cycling of charge–discharge (Figure 4c; Figure S6, Supporting Information). In addition, the

low resistance may be related with the higher N doping level and the larger interlayer distance of NS-CNT-1000.<sup>[42]</sup> Figure 4d evaluates the rate capability of NS-CNT-*T* at different current densities varied in the range of  $0.02$  to  $5.0 \text{ A g}^{-1}$ . It can be seen that NS-CNT-1000 demonstrates high rate tolerance, achieving the capacity of  $151 \text{ mA h g}^{-1}$  even at the high current density of  $5.0 \text{ A g}^{-1}$ . With the current density restored to  $0.02 \text{ A g}^{-1}$ , NS-CNT-1000 still maintains a highly reversible capacity of  $370 \text{ mA h g}^{-1}$ , confirming its remarkable structural stability. On the contrary, NS-CNT-900 and NS-CNT-1100 exhibit much lower capacities at high current densities (Figure 4d). The superior electrochemical performance of NS-CNT-1000 can be attributed

to the highly exposed surfaces, hierarchical pore structure, and the suitable heteroatom doping level, particularly the high ratio of pyrrolic-N species, which prominently provides more adsorption sites for the stable K-ion storage. Meanwhile, N and S co-doping creates defective structures to the carbon nanotubes, hence increasing the hydrophilicity and the wettability of the carbon surface in liquid electrolyte. Moreover, NS-CNT-1000 displays relatively large specific capacities of 188 and 151 mA h g<sup>-1</sup> at the high current densities of 2.0 and 5.0 A g<sup>-1</sup>, respectively (Figure 4d). The enhanced performance at such high current densities could be attributed to the increased interlayer distance in NS-CNT-1000 because the larger interlayer distance in the carbon network enables facile diffusion of the large K-ions. NS-CNT-1000 also exhibits an impressive cycling performance with 98% of its capacity retained even after 500 cycles at 2.0 A g<sup>-1</sup>.

The electrochemical kinetics of NS-CNT-1000 for the K-ion storage were next investigated based on the CV curves obtained at different sweep rates (Figure 5a). All the CV curves show the similar shape with good reversibility at the varied current densities, implying the fast capacitive feature with high stability. Figure 5b displays the *b*-values of ≈0.8 for NS-CNT-1000, suggesting that it exhibits a hybrid process of the capacitive behavior and the diffusion process for the K-ion storage as the N, S co-doped carbon anodes. The sweep rate (*v*) and current (*i*) obey the power-law equation as shown in Equation (1).<sup>[43–45]</sup> The quantification of the capacity contribution ratio could be further derived from the Equation (2):

$$i = av^b \quad (1)$$

$$i(V) = k_1v + k_2v^{1/2} \quad (2)$$

Generally, the *b*-value near to 1.0 indicates a capacitive dominated process, whereas that close to 0.5 represents the diffusion-controlled behavior.<sup>[45]</sup> *k*<sub>1</sub>*v* is related to the capacitive-contribution process and *k*<sub>2</sub>*v*<sup>1/2</sup> is related to diffusion-contribution process.<sup>[46,47]</sup> From the CV profile in Figure 5c, 79.3% of the capacity is derived from the capacitive behavior for NS-CNT-1000 at a scan rate of 1.0 mV s<sup>-1</sup> (blue region). Moreover, as shown in Figure 5d, there is a gradual increase of the capacitive contribution ratio for NS-CNT-1000 from 55.1% (0.1 mV s<sup>-1</sup>) to 79.3% (1.0 mV s<sup>-1</sup>). NS-CNT-1000 shows the largest capacitive contribution ratio at the same sweep ratio as compared to other samples (Figure S8, Supporting Information). NS-CNT-1000 demonstrates the highest rate capabilities at the high current density leading to the enhanced rate capacity. This is potentially due to the microstructures of the NS-CNT-1000 possessing much more micropores inside as previously demonstrated by its NL-DFT pore size distribution (Figure 2d, Table 1). The pore size and pore volume are significant factors influencing the performance of the K-ion storage at the high current density.<sup>[48]</sup> In addition, the synergistic effect of both N and S doping in the NS-CNT with large interlayer distance, hierarchical pore structure, and defective surface also boost the electrochemical performance for potassium ion storage. As an anode electrode material for KIBs, NS-CNT-1000 exhibits excellent performance in the cycling stability and rate capability much greater than that of other carbon samples as shown in Figure S9, Supporting Information.<sup>[42,43,49–52]</sup>

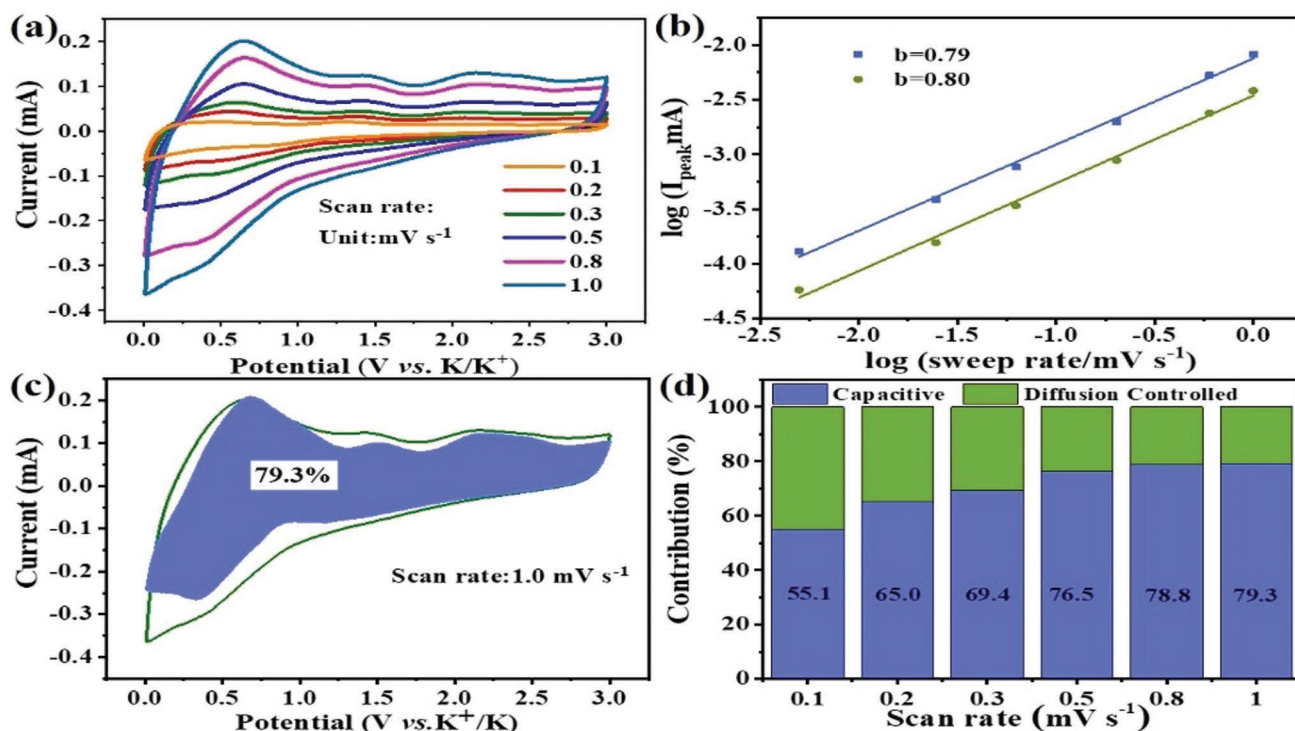


**Figure 5.** CV curves and the corresponding kinetics analysis of NS-CNT-1000. a) CV curves with scan rate varying from 0.1 to 1.0 mV s<sup>-1</sup>, b) *b*-value according to the relationship of the scan rate and peak current, c) CV curve (1.0 mV s<sup>-1</sup>) with the blue area representing the capacitive contribution, and d) capacity at different scan rate with the blue area standing for the capacitive contribution and the green part describing the diffusion-controlled capacity.

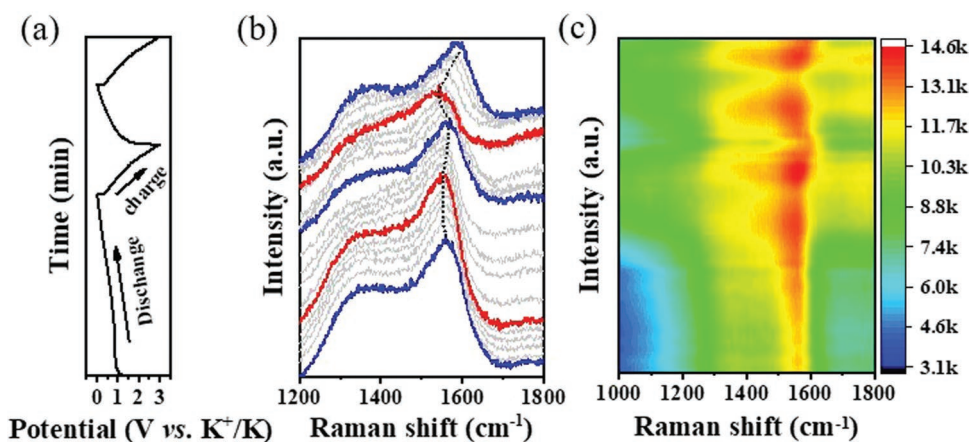


**Figure 6.** a) Corresponding charge/discharge profile from 0.0 to 3.0 V, b) in situ Raman spectra, and c) 2D contour topographic map during charge–discharge of NS-CNT-1000.

To further elucidate the structural stability and reversibility of NS-CNT-1000 for K-ion storage, the characterized G and D bands are recorded via the in situ Raman spectroscopy. As shown in **Figure 6a,b**, the typical G band vibrates regularly with the discharge/charge process, displaying a shift to the lower range in the G band as being discharged from the open circuit voltage (OCV) to 0.01 V and reversely shifts to the higher range as being charged to 3.0 V. The highly reversible shift behavior in the G band reveals the high structural stability of the interlayers in the NS-CNT-1000 carbon network, allowing extremely stable reversibility for K-ion insertion/extraction during discharge/charge. The topographic plot profile in **Figure 6c** clearly demonstrates the reversible evolution in the G band during the discharge/charge process. The ex situ TEM image also demonstrates that NS-CNT-1000 still maintains a good nanotube morphology after the electrochem-

ical testing (**Figure S10**, Supporting Information). This further proves its excellent structural stability, which can be attributed to the unique hollow-tube structure buffering the deformation and the structure destruction upon repeated charge/discharge processes.

DFT calculation was explored for a deeper understanding of the contribution of N, S co-doping to the K-ion storage performance. We first optimized structures of carbon nanotube (CNT) and N–S doped CNT, and then calculated the binding energy ( $E_b$ ) of the K atom embedded into the two structures to characterize the adsorption capacity. **Figure 7a,b** shows the adsorption configurations, and the most energetically stable  $E_b$  of K atom on CNT is calculated to be  $-0.76$  eV. The structure of CNT is slightly deformed after introducing N and S doping in it, while the  $E_b$  increases to 2.13 eV. These results show that the structure of N, S co-doped CNT provides more conducive

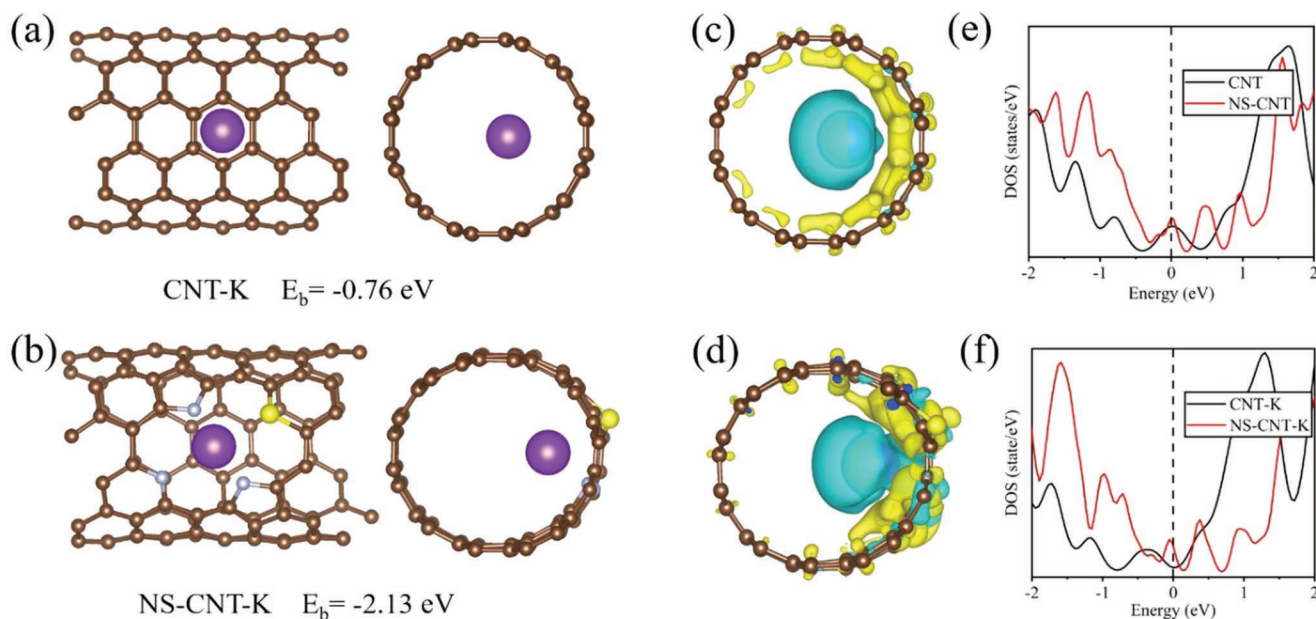


**Figure 7.** Absorption of single K atom in a) CNT and b) NS-CNT structures from top and side view. Electron density differences of c) CNT and d) NS-CNT structures with absorption of single K atom. DOS of e) CNT and f) NS-CNT structures with and without single K atom absorption.

local atomic environment for the adsorption of K ions, thus, promoting the capacity increase in KIB anode materials.

To elucidate the charge density variation with the adsorption of K atom, the bonding charge density with and without adsorption of K atom is calculated. As depicted in Figure 7c,d, where cyan and yellow colors depict the electron depletion and accumulation, respectively, an obvious charge depletion adjacent to the K atom is identified in both cases. This indicates a charge transfer from K atoms to the neighboring atoms, indicating the ionic properties of the bond. There is a more prominent charge accumulation on the N, S co-doped structure than that on CNT, indicating that N, S co-doping endows an enhanced K-ion adsorption capability. Furthermore, we studied the density of states (DOS) of CNT and N–S doped CNT before and after the adsorption of the K atom. As shown in Figure 7e,f, the DOS of N, S co-doped structure near Fermi level increases after the adsorption of K atom versus pristine CNT, indicating that electronic conductivity increases after N–S doping. The above results from the DFT calculation adequately advocate the advantageous role of N, S co-doping for the promotion of the K ion adsorption ability and the improvement of electronic conductivity. It, therefore, offers a favorable explanation for the high specific capacity and excellent rate performance for the NS-CNT electrode.

### 3. Conclusion

This study offers an efficient methodology for the construction of N, S co-doped carbon nanotube. N, S co-doping effectively enhances the performance of K-ion batteries by 1) enlarging the interlayer distance to facilitate the K ion insertion, 2) increasing the electronic conductivity, 3) offering defective sites to promote the K-ion adsorption capability, and 4) enhancing the surface hydrophilicity to increase the wettability with electrolyte. The above advantageous surface efficacy combined with the features of high specific surface area, hierarchical pore structure, and tubular hollow morphology synergistically contribute to the boosted electrochemical performance for potassium ion storage. This work offers a meaningful avenue for the advancement of high-performance carbon material as an anode for K-ion batteries.

### 4. Experimental Section

**Synthesis of CdS Nanowires:** CdS nanowires were synthesized as reported previously.<sup>[53]</sup> In brief, 4.5 g of sodium diethyldithiocarbamate trihydrate and 2.3 g of CdCl<sub>2</sub>·5/2H<sub>2</sub>O were separately added in 40 mL of deionized (DI) water under stirring. The white solids (cadmium diethyldithiocarbamate (Cd(S<sub>2</sub>CNEt<sub>2</sub>)<sub>2</sub>)) were separated via centrifugation and dried at 60 °C overnight. Then, 2.3 g of Cd(S<sub>2</sub>CNEt<sub>2</sub>)<sub>2</sub> was mixed with 60 mL of ethylenediamine in a stainless-steel autoclave with Teflon interlining. After Cd(S<sub>2</sub>CNEt<sub>2</sub>)<sub>2</sub> was completely dissolved, the autoclave was kept at 180 °C for 24 h. A yellowish precipitate was washed with deionized water and ethanol and collected by centrifugation. After drying at 60 °C for 12 h, CdS nanowires were obtained by washing with ethanol and DI water and drying at 60 °C overnight.

**Synthesis of CdS@PDA:** 0.2 g of CdS nanowires was dispersed in the mixture of 400 mL of DI water and 200 mL of ethanol by ultrasonication. 0.4 g of dopamine hydrochloride was subsequently added and the mixture was stirred for 30 min. The polymerization of dopamine was induced by adjusting pH of the mixture to 8.5 with Tris(hydroxymethyl)

aminomethane (Tris-buffer). Subsequent stirring was carried out for 24 h. After the filtration, washing, and drying overnight at 60 °C, CdS@PDA was obtained.

**Synthesis of NS-CNT-T Materials:** 0.2 g of CdS@PDA was evenly dispersed in 40 mL of DI water under ultrasonication. Then, 1.2 g of urea was added to the dispersion of CdS@PDA, and the mixture was dried by stirring at 80 °C. Grey-white CdS@CN powder was obtained. Next, CdS@CN was calcined for 3 h at different temperature under Ar atmosphere to obtain the final product, named NS-CNT-T (where T represents the calcination temperature of 900 °C, 1000 °C, and 1100 °C).

**Characterizations:** Transmission electron microscopy (TEM) images were obtained by JEM-2100F operating at 200 kV. Scanning transmission electron microscope (STEM) images were acquired by a FEI Tecnai C<sup>2</sup> F30 operating at 300 kV. Field-emission scanning electron microscopy (FE-SEM) was performed on JEOL JSM-7800F with an accelerating voltage of 10 kV. X-ray photoelectron spectroscopy (XPS) was conducted by PHI 5000 Versa Probe III with Al-K $\alpha$  X-ray source at 15 kV. X-ray diffraction (XRD) spectra were measured by Rigaku Ultima IV with Cu-K $\alpha$  radiation ( $\lambda = 0.15418$  nm). Thermogravimetric analysis (TGA) was conducted by Mettler toledo SDT Q600 with Ar atmosphere (the heating rate was set at 10 °C min<sup>-1</sup>). Raman spectra were recorded using Renishaw in Via Raman spectrometer with a laser beam source having wavelength of 532 nm. N<sub>2</sub>-sorption experiment was conducted using Quantachrome Autosorb-iQ2. The specific surface area was evaluated by Brunauer–Emmett–Teller (BET) model and Non-Local-Density-Functional-Theory (NL-DFT) was used to estimate the pore size distribution.

**Electrochemical Performance:** Electrochemical performance was investigated with CR-2032 coin cells. NS-CNT-T was blended with carbon black and polyvinylidene fluoride (PVDF) (Solvay S.A.) binder with a mass ratio of 8:1:1. The homogeneous slurry was uniformly coated onto copper foil with a doctor blade. The electrode was dried at 110 °C in a vacuum oven for 12 h. All cells were assembled in Ar protected glove box (H<sub>2</sub>O, O<sub>2</sub> < 0.01 ppm) with 3 m bis(fluorosulfonyl)imide (KFSI) in dimethyl ether (DME) as the electrolyte. Cyclic voltammetry (CV) was tested by CHI 610E electrochemistry workstation (Shanghai Chenhua Co.) with the voltage ranging from 0.01 to 3.0 V. Galvanostatic charge/discharge (GCD) was recorded using Neware instrument (CT-4008) with voltage range of 0.01–3.0 V. Electrochemical impedance spectroscopy (EIS) was performed with frequency varied from 0.01 Hz to 100 kHz. The above tests were all carried out at room temperature.

**Theoretical Calculation Methods:** The projector augmented wave (PAW) method of Vienna ab initio simulation package (VASP) software was used for first-principles calculations.<sup>[54,55]</sup> The cutoff energy of the plane wave basis was set to 550 eV, and the exchange correlation functional adopted Perdew–Burke–Ernzerhof (PBE) functional.<sup>[56]</sup> With the long-range dispersion correction by Grimme (DFT-D2 method), Van der Waals (VdW) interactions were taken into account.<sup>[57]</sup> The reciprocal space of the unit cell was represented by a 2 × 2 × 4 Monkhorst-Pack k-point mesh. The structures were fully optimized, and the energy and force convergence criteria were set to be 10<sup>-6</sup> eV and 0.01 eV Å<sup>-1</sup>, respectively. The binding energy of E<sub>b</sub> was defined as E<sub>b</sub> = E<sub>tot</sub> – E<sub>sub</sub> – E<sub>k</sub>, where E<sub>tot</sub> is the total energy of K adsorption structure, E<sub>sub</sub> is the energy of each substrate, and E<sub>k</sub> is the energy of each K atom in the bulk K metal.

### Supporting Information

Supporting Information is available from the Wiley Online Library or from the author.

### Acknowledgements

X.J. and X.W. contributed equally to this work. This manuscript was financially supported by the National Natural Foundation of China (22072069, 51902170), the Natural Science Foundation of Shandong Province, China (ZR2019YQ08), the Open Project of Key Laboratory



of Green Chemical Engineering Process of the Ministry of Education (GCP20200204), the Open Project of Key Laboratory for Ultrafine Materials of the Ministry of Education, Key Laboratory of Coal Science and Technology, Education Ministry and Shanxi Province, Taiyuan University of Technology (MKX202005), the ARC-Linkage (LP180100429), and the JST-ERATO Yamauchi Materials Space-Tectonics Project (Grant Number: JPMJER2003). B.Y. acknowledges the financial support from Institut Teknologi Bandung (ITB) International Collaboration Research Grant 2022. This work was performed in part at the Queensland node of the Australian National Fabrication Facility, a company established under the National Collaborative Research Infrastructure Strategy to provide nano and microfabrication facilities for Australia's researchers.

Open access publishing facilitated by The University of Queensland, as part of the Wiley - The University of Queensland agreement via the Council of Australian University Librarians.

## Conflict of Interest

The authors declare no conflict of interest.

## Data Availability Statement

The data that support the findings of this study are available on request from the corresponding author. The data are not publicly available due to privacy or ethical restrictions.

## Keywords

carbon nanotubes, fast kinetics, N and S co-doping, potassium ion storage

Received: June 7, 2022

Revised: July 26, 2022

Published online: September 23, 2022

- [1] E. Fan, L. Li, Z. Wang, J. Lin, Y. Huang, Y. Yao, R. Chen, F. Wu, *Chem. Rev.* **2020**, *120*, 7020.
- [2] Y. Qiu, X. Zhang, H. Han, Z. Liu, J. Liu, X. Ji, *J. Power Sources* **2021**, *499*, 229941.
- [3] J. Li, H. Yuan, J. Li, W. Zhang, Y. Liu, N. Liu, H. Cao, Z. Jiao, *Appl. Catal., B* **2021**, *285*, 119833.
- [4] G. Li, H. Chen, B. Zhang, H. Guo, S. Chen, X. Chang, X. Wu, J. Zheng, X. Li, *Appl. Surf. Sci.* **2022**, *582*, 152404.
- [5] B. Zhu, G. Guo, G. Wu, Y. Zhang, A. Dong, J. Hu, D. Yang, *J. Alloys Compd.* **2019**, *775*, 776.
- [6] C. Sun, S. Liu, X. Shi, C. Lai, J. Liang, Y. Chen, *Chem. Eng. J.* **2020**, *381*, 122641.
- [7] C. Wang, J. Zhang, X. Wang, C. Lin, X. S. Zhao, *Adv. Funct. Mater.* **2020**, *30*, 2002629.
- [8] Y. Liu, C. Ding, P. Xie, X. Yan, M. Feng, Y. Liu, C. Liu, Y. Yu, Y. Lin, *Mater. Chem. Front.* **2021**, *5*, 3216.
- [9] Q. Shen, P. Jiang, H. He, Y. Feng, Y. Cai, D. Lei, M. Cai, M. Zhang, *Energy Environ. Mater.* **2021**, *4*, 638.
- [10] H. Kim, J. C. Kim, M. Bianchini, D.-H. Seo, J. Rodriguez-Garcia, G. Ceder, *Adv. Energy Mater.* **2018**, *8*, 1702384.
- [11] S. Dhir, S. Wheeler, I. Capone, M. Pasta, *Chem* **2020**, *6*, 2442.
- [12] W. Feng, N. Feng, W. Liu, Y. Cui, C. Chen, T. Dong, S. Liu, W. Deng, H. Wang, Y. Jin, *Adv. Energy Mater.* **2021**, *11*, 2003215.
- [13] C. Zeng, F. Xie, X. Yang, M. Jaroniec, L. Zhang, S.-Z. Qiao, *Angew. Chem., Int. Ed.* **2018**, *57*, 8540.
- [14] S. Chong, S. Qiao, X. Wei, T. Li, L. Yuan, S. Dong, W. Huang, *iScience* **2021**, *24*, 103494.
- [15] L. Xing, K. Han, Q. Liu, Z. Liu, J. Chu, L. Zhang, X. Ma, Y. Bao, P. Li, W. Wang, *Energy Storage Mater.* **2021**, *36*, 309.
- [16] Y. Liu, C. Yang, Q. Pan, Y. Li, G. Wang, X. Ou, F. Zheng, X. Xiong, M. Liu, Q. Zhang, *J. Mater. Chem. A* **2018**, *6*, 15162.
- [17] Y. He, J. Xue, M. Yang, T. Huang, X. Xia, Y. Chen, H. Liu, *Chem. Eng. J.* **2021**, *409*, 127383.
- [18] S. Alvin, C. Chandra, J. Kim, *Chem. Eng. J.* **2021**, *411*, 128490.
- [19] M. Chen, W. Wang, X. Liang, S. Gong, J. Liu, Q. Wang, S. Guo, H. Yang, *Adv. Energy Mater.* **2018**, *8*, 1800171.
- [20] Y. Liu, H. Dai, Y. An, L. Fu, Q. An, Y. Wu, *J. Mater. Chem. A* **2020**, *8*, 14993.
- [21] S. Tian, Y. Wang, T. Cai, D. Kong, D. Wang, H. Ren, W. Xing, *Appl. Surf. Sci.* **2020**, *534*, 147635.
- [22] Q. Wang, K. Ye, L. Xu, W. Hu, Y. Lei, Y. Zhang, Y. Chen, K. Zhou, J. Jiang, J. M. Basset, D. Wang, Y. Li, *Chem. Commun.* **2019**, *55*, 14801.
- [23] C. Ma, H. Yang, Z. Xu, Z. Fu, Y. Xie, H. Zhang, M. Hong, Z. Ma, H. Xiong, X.-Z. Yuan, *J. Mater. Chem. A* **2020**, *8*, 2836.
- [24] W. Zhang, X. Jiang, Y. Zhao, A. Carné-Sánchez, V. Malgras, J. Kim, J. H. Kim, S. Wang, J. Liu, J.-S. Jiang, Y. Yamauchi, M. Hu, *Chem. Sci.* **2017**, *8*, 3538.
- [25] Y. Bai, Y. Liu, Y. Li, L. Ling, F. Wu, C. Wu, *RSC Adv.* **2017**, *7*, 5519.
- [26] M. Kim, J. F. S. Fernando, Z. Li, A. Alowasheer, A. Ashok, R. Xin, D. Martin, A. K. Nanjundan, D. V. Golberg, Y. Yamauchi, N. Amiralian, J. Li, *Chem. Eng. J.* **2022**, *445*, 136344.
- [27] Y. Tan, C. Yang, W. Qian, C. Teng, *J. Alloys Compd.* **2020**, *826*, 154133.
- [28] M. Kim, J. F. S. Fernando, J. Wang, A. K. Nanjundan, J. Na, M. S. A. Hossain, H. Nara, D. Martin, Y. Sugahara, D. Golberg, Y. Yamauchi, *Chem. Commun.* **2022**, *58*, 863.
- [29] M. Yu, Z. Yin, G. Yan, Z. Wang, H. Guo, G. Li, Y. Liu, L. Li, J. Wang, *J. Power Sources* **2020**, *449*, 227514.
- [30] M. Kim, X. Xu, R. Xin, J. Earnshaw, A. Ashok, J. Kim, T. Park, A. K. Nanjundan, W. A. El-Said, J. W. Yi, J. Na, Y. Yamauchi, *ACS Appl. Mater. Interfaces* **2021**, *13*, 52034.
- [31] M. Kim, T. Park, C. Wang, J. Tang, H. Lim, M. S. A. Hossain, M. Konarova, J. W. Yi, J. Na, J. Kim, Y. Yamauchi, *ACS Appl. Mater. Interfaces* **2020**, *12*, 34065.
- [32] X. Xu, H. Zeng, D. Han, K. Qiao, W. Xing, M. J. Rood, Z. Yan, *ACS Appl. Mater. Interfaces* **2018**, *10*, 37172.
- [33] G. Zou, H. Hou, C. W. Foster, C. E. Banks, T. Guo, Y. Jiang, Y. Zhang, X. Ji, *Adv. Sci.* **2018**, *5*, 1800241.
- [34] J. Ye, H. Zhao, W. Song, N. Wang, M. Kang, Z. Li, *J. Power Sources* **2019**, *412*, 606.
- [35] J. Yang, X. Zhou, D. Wu, X. Zhao, Z. Zhou, *Adv. Mater.* **2017**, *29*, 1604108.
- [36] M. Zhang, M. Shoaib, H. Fei, T. Wang, J. Zhong, L. Fan, L. Wang, H. Luo, S. Tan, Y. Wang, J. Zhu, J. Hu, B. Lu, *Adv. Energy Mater.* **2019**, *9*, 1901663.
- [37] B. Yang, J. Chen, L. Liu, P. Ma, B. Liu, J. Lang, Y. Tang, X. Yan, *Energy Storage Mater.* **2019**, *23*, 522.
- [38] W. Cha, I. Y. Kim, J. M. Lee, S. Kim, K. Ramadass, K. Gopalakrishnan, S. Premkumar, S. Umamathy, A. Vinu, *ACS Appl. Mater. Interfaces* **2019**, *11*, 27192.
- [39] Q. Wang, X. Ge, J. Xu, Y. Du, X. Zhao, L. Si, X. Zhou, *ACS Appl. Energy Mater.* **2018**, *1*, 6638.
- [40] B. Quan, A. Jin, S.-H. Yu, S. M. Kang, J. Jeong, H. D. Abruña, L. Jin, Y. Piao, Y.-E. Sung, *Adv. Sci.* **2018**, *5*, 1700880.
- [41] J. Yang, Z. Ju, Y. Jiang, Z. Xing, B. Xi, J. Feng, S. Xiong, *Adv. Mater.* **2018**, *30*, 1700104.
- [42] L. Liu, Y. Chen, Y. Xie, P. Tao, Q. Li, C. Yan, *Adv. Funct. Mater.* **2018**, *28*, 1801989.
- [43] Y. Cui, W. Liu, X. Wang, J. Li, Y. Zhang, Y. Du, S. Liu, H. Wang, W. Feng, M. Chen, *ACS Nano* **2019**, *13*, 11582.

- [44] Z. Yi, Y. Qian, S. Jiang, Y. Li, N. Lin, Y. Qian, *Chem. Eng. J.* **2020**, 379, 122352.
- [45] W. Yang, J. Zhou, S. Wang, Z. Wang, F. Lv, W. Zhang, W. Zhang, Q. Sun, S. Guo, *ACS Energy Lett.* **2020**, 5, 1653.
- [46] Y. Cui, W. Liu, W. Feng, Y. Zhang, Y. Du, S. Liu, H. Wang, M. Chen, J. Zhou, *Adv. Funct. Mater.* **2020**, 30, 1908755.
- [47] N. Fu, Y. Liu, R. Liu, X. Wang, Z. Yang, *Small* **2020**, 16, 2001607.
- [48] S. Y. Li, W. H. Li, X. L. Wu, Y. Tian, J. Yue, G. Zhu, *Chem. Sci.* **2019**, 10, 7695.
- [49] X. Hu, Y. Liu, J. Chen, L. Yi, H. Zhan, Z. Wen, *Adv. Energy Mater.* **2019**, 9, 1901533.
- [50] J. Lu, C. Wang, H. Yu, S. Gong, G. Xia, P. Jiang, P. Xu, K. Yang, Q. Chen, *Adv. Funct. Mater.* **2019**, 29, 1906126.
- [51] M. Liu, L. Chang, J. Wang, J. Li, J. Jiang, G. Pang, H. Wang, P. Nie, C. Zhao, T. Xu, L. Wang, *J. Power Sources* **2020**, 469, 228415.
- [52] P. Xiong, X. Zhao, Y. Xu, *ChemSusChem* **2018**, 11, 202.
- [53] I. Sultana, T. Ramireddy, M. M. Rahman, Y. Chen, A. M. Glushenkov, *Chem. Commun.* **2016**, 52, 9279.
- [54] G. Kresse, J. Furthmüller, *Phys. Rev. B* **1996**, 54, 11169.
- [55] G. Kresse, D. Joubert, *Phys. Rev. B* **1999**, 59, 1758.
- [56] J. P. Perdew, K. Burke, M. Ernzerhof, *Phys. Rev. Lett.* **1996**, 77, 3865.
- [57] S. Grimme, *J. Comput. Chem.* **2006**, 27, 1787.